Title	Structure and crystallization behavior of Na_2O-ZrO_2-SiO_2-P_2O_5 glass for solid-state electrolyte separation
Author(s)	Sakaeda, Kento; Shinozaki, Kenji; Kitta, Mitsunori et al.
Citation	Journal of Non-Crystalline Solids. 2024, 638, p. 123070
Version Type	VoR
URL	https://hdl.handle.net/11094/97656
rights	This article is licensed under a Creative Commons Attribution 4.0 International License.
Note	
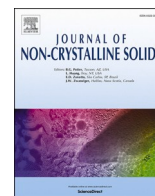
Structure and crystallization behavior of Na$_2$O–ZrO$_2$–SiO$_2$–P$_2$O$_5$ glass for solid-state electrolyte separation

Kento Sakaeda [a],[b], Kenji Shinozaki [a],[b],[*], Mitsunori Kitta [c], Yuuki Kitagawa [a], Sohei Sukenaga [d], Tsuyoshi Honma [e]

[a] Nanomaterials Research Institute, Department of Materials and Chemistry, National Institute of Advanced Industrial Science and Technology (AIST), Ikeda, Osaka 563-8577, Japan
[b] Graduate School of Engineering, Osaka University, Suita, Osaka 565-0871, Japan
[c] Research Institute of Electrochemical Energy, Department of Energy and Environment, National Institute of Advanced Industrial Science and Technology (AIST), Ikeda, Osaka 563-8577, Japan
[d] Institute of Multidisciplinary Research for Advanced Materials, Tohoku University, 2-1-1 Katahira, Aoba-ku, Sendai, Miyagi 980-8577, Japan
[e] Department of Materials Science and Bioengineering, Nagaoka University of Technology, Nagaoka, Niigata 940-2188, Japan

ARTICLE INFO

ABSTRACT

Glass ceramics containing Na super-ionic conductor (NASICON) crystals are promising candidates for solid-state electrolyte separators in aqueous sodium ion batteries due to their high ion conductivity, water stability, and productivity. Our objective was to fabricate a glass-ceramic separator by crystallizing a NASICON phase within the glass via heat-treatment. We conducted a detailed investigation into the structural evolution of the glass and the crystallization morphology. Upon heat-treatment, Si units polymerized to form an island-like phase, while P contributed to increasing non-bridging O to form a sea-like phase during droplet phase separation; subsequently, the Na$_2$Zr$_2$SiP$_2$O$_{12}$ crystalline phase formed. The remaining glass comprised Q^4 units of Si in the island-like phase, and Q^1 and Q^2 units of P in the sea-like phase. The ionic conductivity of the sample increased by crystallization up to 5.4×10^{-5} S·cm^{-1} at 300 K. Furthermore, the water leakage tests showed that both the glass and glass-ceramics exhibited low leakages.

1. Introduction

Aqueous sodium-ion batteries (A-SIBs) are poised to become next-generation batteries owing to their remarkable safety features, cost advantages [1,2], and the abundance of natural Na resources. A-SIBs are expected to play pivotal roles in various scales of stationary secondary battery applications, facilitating diverse functions in the development of electrical energy storage systems [3].

However, the choice of electrode materials in A-SIBs is constrained by the narrow electrochemical potential window of water (1.23 V). Therefore, extensive efforts have been undertaken to widen this potential window by employing highly concentrated salt solutions [4–9]; nevertheless, this remains insufficient for negative-electrode materials operating at a lower potential [10]. A promising method to widen the potential window of water in A-SIBs involves the utilization of a solid separator that selectively enables the passage of Na while blocking water and protons. Moreover, solid separators are promising for the realization of seawater rechargeable batteries [3].

β-alumina and sulfide systems exhibit potential as solid-state electrolyte separators with high ion conductivity in SIBs [11]. However, they are not suitable for A-SIBs due to their poor water stability. In contrast, Na super-ionic conductor (NASICON) systems are promising separators for A-SIBs owing to their high ion conductivity and water stability [12–14]. However, NASICON single crystals and fully dense polycrystalline materials are prohibitively expensive for practical applications, which undermines the crucial advantage of A-SIBs, i.e., their affordability. Moreover, the sintering of NASICON materials mixed with glass has proven insufficient to achieve complete densification for preventing water ingress effectively [15].

Glass without cracks or pores that molecular water pass through can be easily prepared over large areas. To achieve high conductivity and densification, Susman et al. [16,17] fabricated glasses with compositions similar to that of Na$_{x+1}$Zr$_2$Si$_x$P$_{3-x}$O$_{12}$ (NZSP) The Na-ion conductivity (σ) of the glass was $1.1–1.9 \times 10^{-3}$ S·cm^{-1} at 573 K, which is below that of an NZSP crystal (2.5×10^{-2} S·cm^{-1} at 573 K). Compared to the aforementioned glass, glass-ceramics with approximately one order of

magnitude higher ionic conductivity have been fabricated by crystallizing (via heat-treatment) an NZSP phase in Na_2O–ZrO_2–SiO_2–P_2O_5 glasses [18]. NZSP-type glass-ceramics are anticipated to provide solid-state electrolytes with high Na-ion conductivity, water resistance, and water impermeability. In the case of $20Na_2O$–$XZrO_2$–$(80–X–Y)$ SiO_2–YP_2O_5 (in mol%) system, the hexagonal phase with $X = 1.1$–1.4 precipitated, whereas in the case of $30Na_2O$–$XZrO_2$–$(70–X–Y)SiO_2$–YP_2O_5 (in mol%) system, the monoclinic phase with $X = 1.8$–2.2 precipitated. In both cases, the ionic conductivity increased 1–2 orders of magnitude after crystallization. The hexagonal phase formed a continuous structure, whereas the monoclinic phase formed in droplets. In this study, we focused on $20Na_2O$–$22.5ZrO_2$–$42.5SiO_2$–$15P_2O_5$ (in mol%) glass, which resulted in a crystallized glass exhibiting the highest conductivity among reported glass systems.

Hence, in this study, we aimed to develop a NASICON separator for A-SIBs, using NZSP-type glass-ceramics. To achieve high Na-ion conductivity in glass-ceramics, appropriate conductive paths must be designed by controlling the crystal morphology. The crystal morphology depends on the crystallization mechanism and the rate of nucleation and growth, which are strongly related to the glass structure [19–23]. This is because nucleation is facilitated in glasses that bear a structural similarity to precipitated crystals. However, the glass structure, crystallization mechanism, detailed morphology, and phases of such crystalline glasses have not been reported thus far. Hence, in this study, the glass structure was investigated via magic angle spinning nuclear magnetic resonance (MAS-NMR) spectroscopy and molecular dynamics (MD) simulations. The interatomic potential was based on graph neural networks (GNN) and three-body interactions [24]. The crystallization process was investigated via transmittance and scanning electron microscopy, and a crystallization mechanism was proposed. Ionic conductivity and water resistance tests were conducted on the glass-ceramics to assess their potential applications in A-SIBs.

2. Experimental

2.1. Sample preparation

Glass ($20Na_2O$–$22.5ZrO_2$–$15P_2O_5$–$42.5SiO_2$ in mol%) samples were prepared via a conventional melt-quenching method [18]. A mixture (100 g total) of Na_2CO_3 (99.9 %), SiO_2 (99.9 %), ZrO_2 (99.9 %), and NaH_2PO_4 (99.0 %) was placed inside a Pt–Rh crucible and melted at 1650 °C for 1 h under ambient atmosphere. The melts were then poured into a carbon mold and immediately placed in an electric furnace heated to 600 °C, where they underwent gradual cooling. The samples were cut into 15 mm square pieces with a thickness of 1 mm and then mirror-polished. The polished samples were heat-treated at 800, 820, 850, 880, 900, 945, 973, 1060, and 1200 °C for 1 h at a heating and cooling rate of 10 K/min.

2.2. Glass and glass ceramics characterization

The glass transition temperature (T_g) and crystallization temperature (T_p) of the samples were determined via differential thermal analysis (DTA) at a heating rate of 10 K/min. The crystalline phases of the samples were determined via high-temperature X-ray diffraction (XRD) employing a Cu-Kα source (Ultima IV; Rigaku, Japan) and synchrotron XRD conducted on the beamline BL-02B2 at SPring-8 (Sayo-cho, Japan) at 20 keV. The X-ray wavelength was calibrated using CeO_2 as a reference material. The XRD patterns of the crystalline phases were simulated utilizing VESTA [25].

Transmission electron microscopy (TEM) and scanning transmission electron microscopy (STEM) were performed employing a JEM-2100 Plus (Hitachi High Tech., Japan). The samples were individually crushed and dispersed on a Cu grid for observation. The elemental distributions were surveyed through an energy-dispersive spectroscopy (EDS) unit equipped on the STEM instrument. The morphologies of the precipitated crystals were observed using field-emission scanning electron microscopy (FE-SEM, Regulus 8220, HITACHI, Co., Ltd.).

The structures of the glass and glass-ceramics were examined using MAS-NMR. Silicon-29 (^{29}Si) and phosphorus-31(^{31}P) MAS-NMR measurements were performed using JEOL ECA-300 (1 T, 300 MHz) at a spinning rate of 10 kHz. The signals were collected using a single-pulse sequence at a tip angle of 30°. ^{29}Si NMR and ^{31}P NMR spectra were referenced to tetramethylsilane and 1-M phosphoric acid solution, respectively. The Zr K-edge EXAFS spectroscopy was conducted at the BL14B2 beamline at SPring-8. Furthermore, ZrO_2 was used as the reference sample. All samples were prepared by mixing with boron nitride to an optimum concentration of the target ion. All data were collected in the standard transmission mode using an ion chamber detector.

The ionic conductivities of the glass and glass-ceramic samples were measured via an ion impedance analyzer. Measurements were taken by heating the samples to different temperatures, and the impedance data were converted into Nyquist plots to determine the conductivity. The details of the measurement procedure and setup are described elsewhere [15]. The standard uncertainty of the conductivity was estimated by measuring the same sample three times and confirming that it was less than 5 %. Cyclic voltammetry (CV) was performed to test the leakage into water. The setup and measurement conditions have been outlined in a previous study [12].

To simulate the glass structure, MD simulations were performed using the LAMMPS package [26]. A total of 1440 ions (160 Na, 90 Zr, 170 Si, 120 P, and 900 O) were randomly placed in a cell to measure the experimental density of 2.897 g/cm^3, and a classical MD simulation was conducted with a completely ionic model [27]. The structure was held at 2000 K for 1,000,000 steps and then cooled to 300 K at 0.1 K/ps under the NVT ensemble, with the obtained structure used as the initial structure for GNN-MD simulation through a universal graph deep-learning interatomic potential with the three-body interaction model M3GNET [24]. The structure was held at 2000 K for 100 ps and then cooled to 300 K at 10 K/ps under an NVT ensemble. A further 10,000 steps were performed at 300 K, and the pair distribution functions were calculated. For both simulations, the time interval of an MD step was set to 0.5 fs.

3. Results and discussion

3.1. Crystallization of glass

High-temperature *in situ* and simulated XRD patterns of the NZSP phases obtained under the different heating conditions are shown in Fig. 1 [28,29]. Only a halo is observed up to 850 °C. Peaks begin to appear from 900 °C, with become more distinct at 950 °C. These peaks are attributed to a $Na_{x+1}Zr_2Si_xP_{3-x}O_{12}$ phase, which has several polymorphs depending on the composition and temperature, as summarized in Table 1 [28,29]. The phase transition of $Na_3Zr_2Si_2PO_{12}$ from monoclinic to rhombohedral has been reported to occur at 160–167 °C [30, 31]; hence, synchrotron XRD measurements were conducted to determine the crystal phase of the heat-treated samples at 300 K (Fig. 2). The XRD peak positions exhibited by each heat-treated sample were similar to those of $Na_2Zr_2SiP_2O_{12}$ (rhombohedral, $R3\_c$). The diffraction lines appearing at 5°, 8°, and 11° are those that disappeared in the space group $R3\_c$ based on the annihilation rule. This indicates the occurrence of a metastable crystalline phase with a slightly different symmetry. Notably, metastable phases can be precipitated via the glass crystallization technique [32,33].

The DTA curves of the as-received and heat-treated glass (not crystallized) samples are shown in Fig. 3. The crystallization peaks shift towards a lower temperature as the heat-treatment temperature increases from 800 to 850 °C, where the samples are not crystallized, as shown in Fig. 1. In the case of prior nucleation or crystallization, heat-treating glass at a temperature below its crystallization temperature
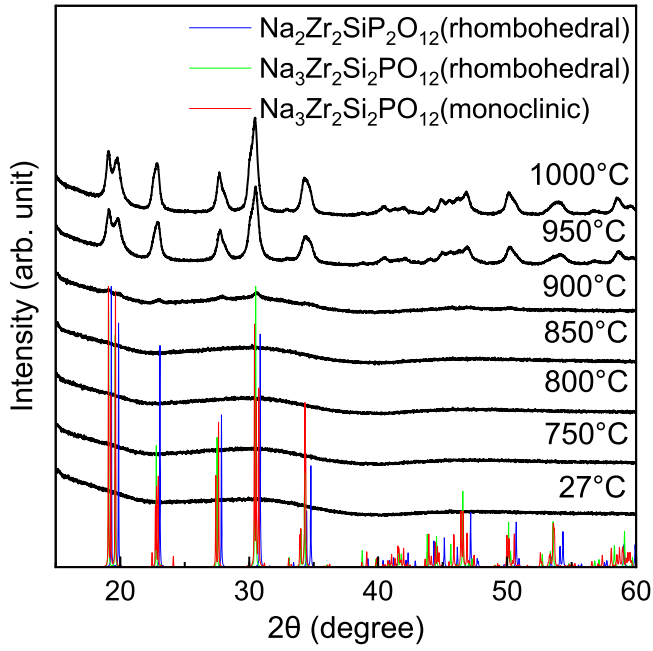
Fig. 1. *In situ* XRD patterns of the glass samples recorded at various temperatures, as indicated by the labels on each pattern.

Fig. 2. Synchrotron XRD patterns of the heat-treated samples. Asterisks (*) indicate where the space group of $Na_2Zr_2SiP_2O_{12}$ changes.

Table 1
Lattice constants of some NZSP crystals.

Phase Structure Space group	$Na_3Zr_2Si_2PO_{12}$ Monoclinic $C2/c$	$Na_3Zr_2Si_2PO_{12}$ Rhombohedral $R\overline{3}\_c$	$Na_2Zr_2SiP_2O_{12}$ Rhombohedral $R\overline{3}\_c$	Glass-ceramics Rhombohedral *Similar to $R\overline{3}\_c$*
a (Å)	15.6513	9.05350	8.9348	8.943 ± 0.005
b (Å)	9.0550	9.05350	8.9348	8.943 ± 0.005
c (Å)	9.2198	23.06770	22.8486	22.873 ± 0.005
α (°)	90	90	90	90
β (°)	123.742	90	90	90
γ (°)	90	120	120	120
ref	25	2	26	This study

decreases the temperature corresponding to the crystallization peak. The nanostructures of the samples heat-treated at 800, 850, 900, and 973 °C were examined via TEM (Fig. 4). Samples heat-treated at temperatures up to 800 °C did not exhibit any nanostructures. Some microstructures seem to separate into a spinodal phase, as observed in the sample heat-treated at 850 °C. The electron diffraction from the TEM analysis and *in situ* high-temperature XRD (Fig. 1) confirmed that the sample was amorphous, suggesting phase separation. Upon further heating, the separated phases crystallized, and the crystals precipitated. These results suggest that the phase separation was induced prior to crystallization and promoted this transformation.

3.2. . Glass structure and local structural change during crystallization

Fig. 5(a) and 5(b) show the structural model obtained through GNN-MD simulation and the obtained pair distribution function $g(r)$, respectively. The coordination number of each atom was calculated using the following equation:

$$CN = \int_0^{r_m} \rho g(r) 4\pi r^2 dr,$$ (1)

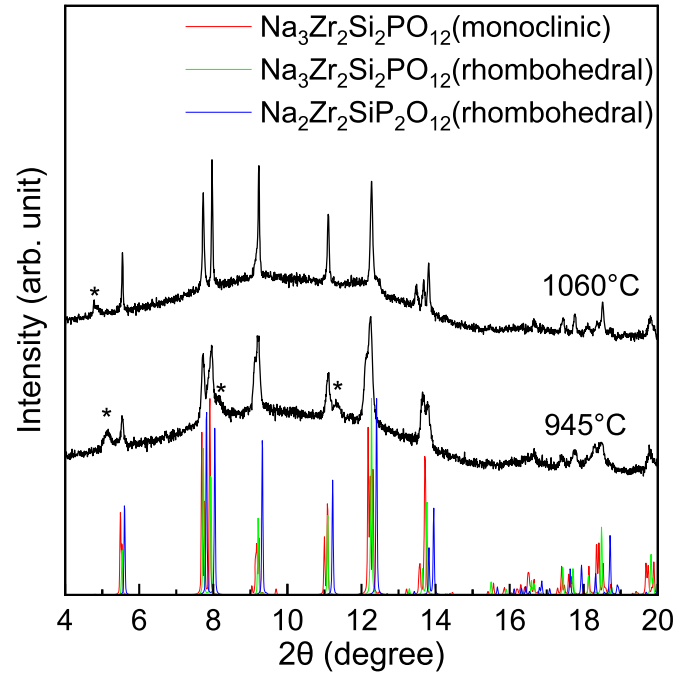where r denotes the average atomic number density calculated from the
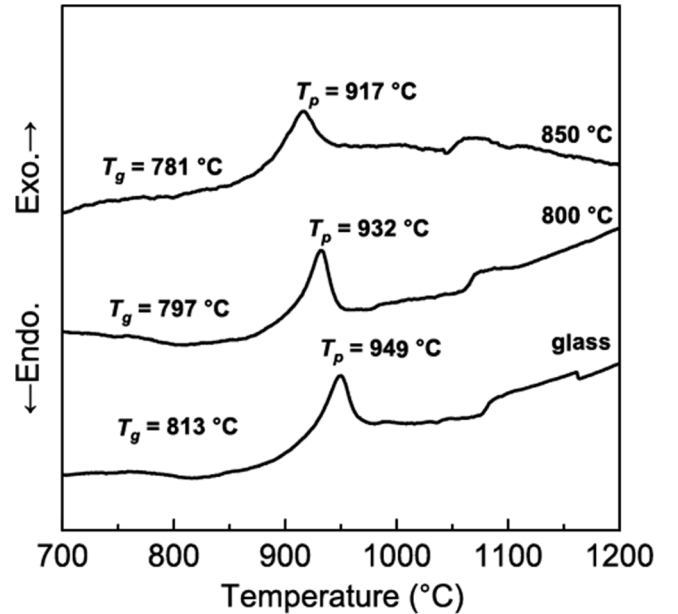

Fig. 3. DTA curves for non-heat-treated glass and samples heat-treated at 800 and 850 °C. The glass transition (T_g) and crystallization peak temperatures (T_p) are also indicated.

MD simulation, r represents the number density, and r_m is the minimum of $g(r)$. The obtained coordination numbers are listed in Table 2. The coordination numbers of Si and P are 4, as typically observed in silicates and phosphates. According to the MD results, the coordination number of Zr is 6, and the Zr–O bond length is 2.065 Å. Zr–O units in glass are known to connect with other units in corner-, edge-, and face-sharing configurations [34]. All the connected Zr–O units in this glass share corners, which does not change during crystallization.

As the structure of the Zr units affects the crystallization behavior, the local structure around Zr was investigated by EXAFS. The k^3-
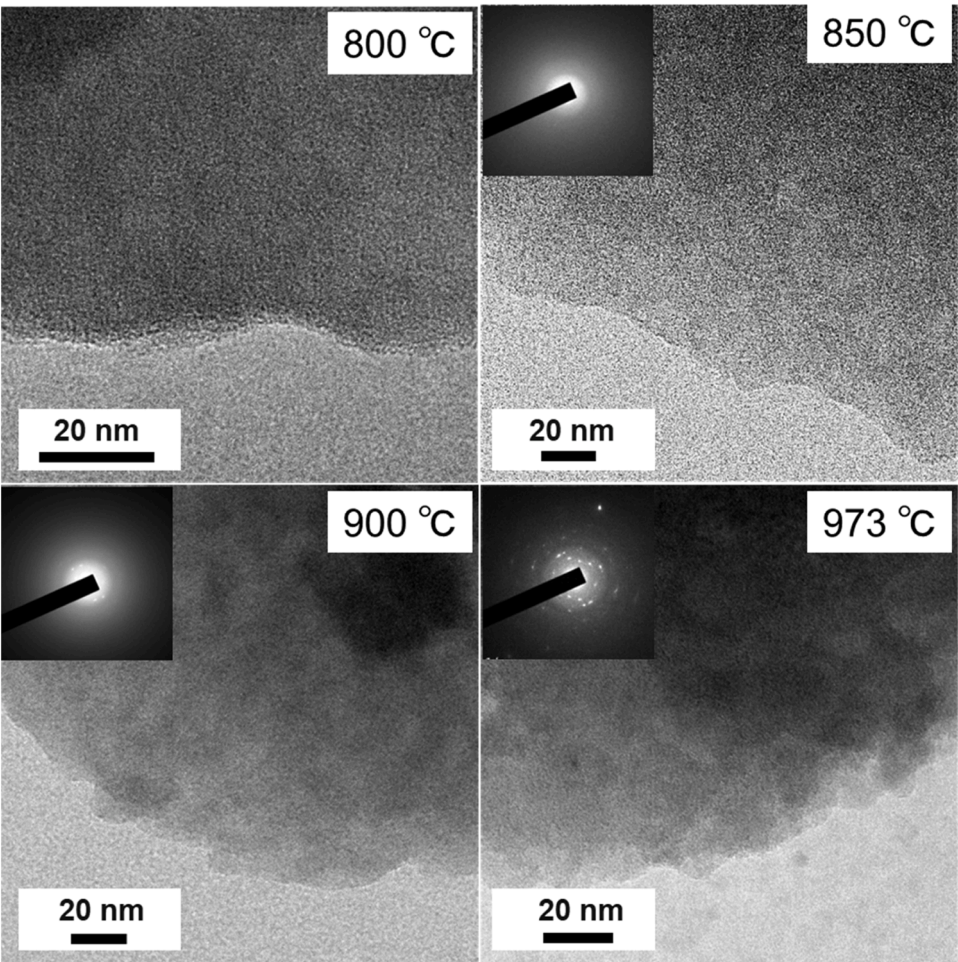
Fig. 4. TEM images of samples heat-treated at 800, 850, 900, and 973 °C. Corresponding electron diffraction patterns are shown in the insets.
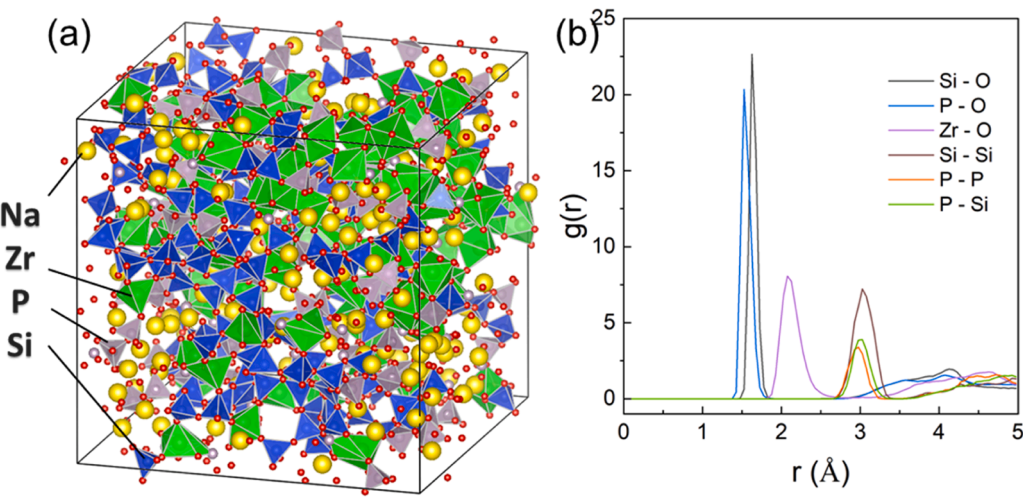

Fig. 5. (a) Structural model obtained through MD simulation with GNN potential and (b) the pair distribution function.

Table 2
Coordination numbers of second neighbor ions.

Si-unit			P-unit		
Si–Si	Si–P	Si–Zr	P–P	P–Si	P–Zr
2.1	0.71	1.1	0.59	1	1.3

weighted EXAFS data and radial distance are shown in Fig. 6. The radial distance of Zr–O in the glass was 2.065 Å. Reportedly, the relationship between the coordination number of atoms and bond length of crystals indicates that Zr coordination numbers of 6 and 8 correspond to a Zr bond length of 2.07 and 2.20 Å, respectively [34]. Therefore, the co-ordination number of Zr in the glass sample is 6. Moreover, the radial distances of Zr do not show any shift by heat-treatment at 850 and 945
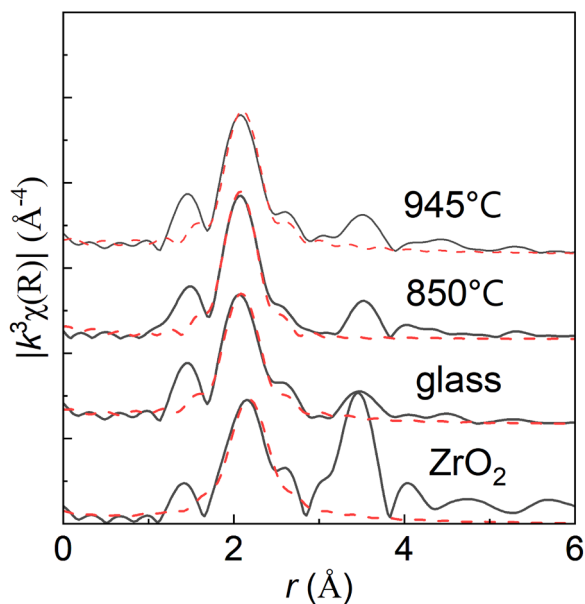
Fig. 6. Experimental radial distance (black solid line), *R*, and fitted curves (red dashed line) calculated by using the first shell model on the Zr K-edge for the non-heat-treated and heat-treated glass samples.

Table 3

Chemical shifts of ^{29}Si for various crystalline phases and the corresponding co-ordination number of Si and Zr.

^{29}Si Chemical shift (ppm)	phase	Q^n	nZr	Ref
−59.0–−59.5	Na$_2$O–SiO$_2$ glass	Q^0	0	[37]
−66.7–−68.0	Na$_2$O–SiO$_2$ glass	Q^1	0	[37]
−75.5–−76.9	Na$_2$O–SiO$_2$ glass	Q^2	0	[37]
−86.5	Na$_4$Zr$_2$Si$_3$O$_{12}$	Q^0	4	[38]
−86.7, −88.9	Na$_2$Si$_2$O$_7$	Q^1	3	[35]
−87.8, −88.2, −88.8	Na$_2$ZrSi$_3$O$_9$ · 2H$_2$O	Q^2	2	[36]
−84.8–−87.1	Na$_2$O–SiO$_2$ glass	Q^3	0	[37]
−90	Na$_3$Zr$_2$Si$_2$PO$_{12}$	Q^0	4	[38]
−95.5	Na$_2$Zr$_2$SiP$_2$O$_{12}$	Q^0	4	[38]
−96.2, −98.2	Na$_2$Si$_4$O$_{11}$	Q^2	2	[35]
−99.0–−105.6	Na$_2$O–SiO$_2$ glass	Q^4	0	[37]
−103, −105, −108	Na$_4$ZrSi$_6$O$_{15}$ · 3H$_2$O	Q^3	1	[35,40]

Table 4

Chemical shifts of ^{31}P for various crystalline phases and the corresponding co-ordination number of Si and Zr.

^{31}P Chemical shift (ppm)	Crystalline phase	Q^n	nZr	Ref
13.8	Na$_3$PO$_4$	Q^0	0	[43]
1.5–2.0	Na$_2$O–P$_2$O$_5$	Q^1	0	[41]
−7.6	(HO)$_3$PO–Zr	Q^0	1	[45]
−11.1	Na$_3$Zr$_2$Si$_2$PO$_{12}$	Q^0	4	[38]
−14.7–−16.7	(HO)$_2$P(O–Zr)$_2$	Q^0	2	[45]
−18.9	Na$_2$Zr$_2$SiP$_2$O$_{12}$	Q^0	4	[38]
−16.9–−26.0	Na$_2$O–P$_2$O$_5$	Q^2	0	[41]
−20.6–−21.3	HOP(O–Zr)$_3$	Q^0	3	[45]
−36.0–−37.9	Na$_2$O–P$_2$O$_5$ glass	Q^3	0	[41]
−24.5	Na$_1$Zr$_2$P$_3$O$_{12}$	Q^0	4	[38]
−30–−46	ZrP$_2$O$_7$	Q^1	3	[46]

°C, indicating that the local structure around Zr is unchanged during crystallization. In other words, the glass has a similar local structure for Zr as the Na$_2$Zr$_2$Si$_2$PO$_{12}$ crystal.

Fig. 7(a) and (b) show the ^{29}Si and ^{31}P MAS-NMR spectra, respectively, of the non-heat-treated glass sample and the samples heat-treated at 850 and 945 °C. Tables 3 and 4 list the chemical shifts of ^{29}Si and ^{31}P in various crystals for different local structures (Q^n). The number of second-neighbor Zr ions and their structures are also shown because the coordination of Zr significantly affects the chemical shift. The ^{29}Si MAS-NMR spectrum of the non-heat-treated glass exhibited a main peak at −89 ppm and shoulder peaks at −87 and −89 ppm, which are attributed to Q^3, Q^2, Q^1, and Q^0 units bonded to 0, 2, 3, and 4 Zr ions, respectively [35–37]. The peaks are positioned too close to each other to be clearly attributed. The MD results suggest that 2.96 Si binds with 0.85 Zr. The difference in polarization between P and Si is small and

indistinguishable by NMR. The MD simulation results suggest that 2.96 of the SiO$_2$ tetrahedra are bonded to Si or P and the rest are non-bridged O. The NMR peaks were too close to each other to be distinguished and attributed; however, a comparison with MD results suggested that the main peaks could be attributed to Q^3 and Q^2. The ^{31}P MAS-NMR for the glass exhibited a peak at −11 ppm and a shoulder peak at −6 ppm, which are primarily attributed to a Q^0 unit bonded to 2 Zr ions and Q^0 units bonded to 1 Zr ion, respectively. The MD simulation results suggested a coordination number of 0.40, 1.1, and 1.5 for P, Si, and Zr, respectively. The Q^n units can be overestimated during the MD
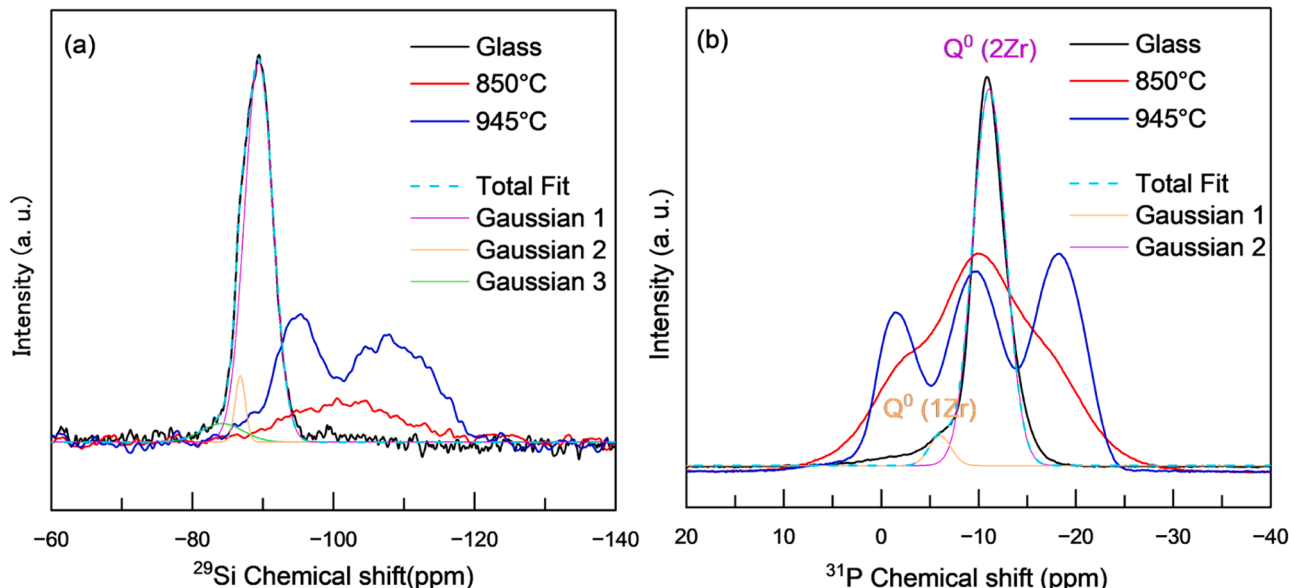

Fig. 7. (a) ^{29}Si and (b) ^{31}P NMR spectra of the as-received samples and samples heat-treated at 850 and 945 °C.

simulation; however, the number of bonded Zr is close to that obtained via MAS-NMR.

After heat-treatment at 850 °C (before crystallization), the ^{29}Si MAS-NMR spectrum of the sample exhibited a broad peak at −102 ppm, indicating mixed chemical shift peaks of Q^4 silicate units with Zr coordination, such as Q^0 (4 Zr), Q^2 (2 Zr), and Q^3 (1 Zr) [35,38–40]. The ^{31}P MAS-NMR spectrum of the heat-treated sample at 850 °C exhibited a broad peak at −10 ppm, which is attributed to a Q^0 unit bonded to 1 or 2 Zr ions [38]. The shoulder peaks at −3 and −18 ppm are assigned to the Q^1 unit and either a Q^0 unit bonded to 3 Zr ions or a Q^2 unit [41,38].

After heat-treatment at 945 °C (after crystallization), the ^{29}Si MAS-NMR spectrum of the sample exhibited peaks at −95 and −108 ppm, which are attributed to a Q^0 unit bonded to 4 Zr ions ($Na_2Zr_2SiP_2O_{12}$) and Q^4 unit [35,38,39,42], respectively. The XRD analysis results identified $Na_{x+1}Zr_2Si_xP_{3-x}O_{12}$ as $Na_2Zr_2SiP_2O_{12}$. The NZSP chemical shift differed with the value of *x*. The chemical shift observed in this study aligns with that of $Na_2Zr_2SiP_2O_{12}$. The peaks in the ^{31}P MAS-NMR spectrum were attributed to a Q^0 unit bonded to 1–4 Zr ions and to Q^1 and Q^2 units [37,38,41,43,44]. The chemical shift was matched to $Na_2Zr_2SiP_2O_{12}$.

Fig. 8 illustrates the structural evolution of the glass samples during heat-treatment, as indicated by the above findings. The non-heat-treated glass sample is composed of Q^2 (2 Zr) and Q^3 units of Si as well as Q^0 (1 Zr, 2 Zr) and Q^1 units of P. Upon heat-treatment below the crystallization temperature, the Si units are converted to silicate units with Zr coordination, such as Q^0 (4 Zr), Q^2 (2 Zr), and Q^3 (1 Zr), and the P units are converted to Q^0 (3 Zr) and Q^2 units. While crystallizing, some of the converted Si and P units transition to the $Na_2Zr_2SiP_2O_{12}$ crystalline phase. The remainder of the glass is composed of Q^4 units of Si and Q^1 and Q^2 units of P, with a Na-rich phase.

3.3. Morphological changes during crystal growth

Fig. 9 shows the FE-SEM images (backscattered electron mode) of the heat-treated samples. No morphological changes are observed in the samples heat-treated below 900 °C owing to insufficient resolution. As shown in Fig. 4, nanophase separation was observed by TEM in the sample heat-treated at 850 °C. Island-like structures appear from 900 °C, and numerous nanocrystal particles with a size of approximately 300 nm are observed within the islands. As the heat-treatment temperature increases, the particles begin to connect, exhibiting a spinodal-like morphology on the island. After heat-treatment at 1200 °C, these crystalline particles adopt a cubic shape.

Fig. 10 (a–h) shows the STEM-EDS maps of the sample heat-treated at 1000 °C. The sample consists of sea- and island-like structures, where the islands are composed of Si-, Na-, and P-rich phases, and the surrounding sea is composed of Na- and P-rich phases. Note that the mapping of P and Zr contains information on the other elements because the characteristic X-ray energies of P and Zr are too similar to be distinguished. Si is abundant in the spheres, and it is considered to have separated from the sea-like structure owing to a phase separation before crystallization. This is because Si and P are known to easily form separate phases, suggesting that the phase separation occurred before crystallization. The Si-rich phase constituting the island has a few other cations, and this phase is believed to contain the Si Q^4 units suggested by NMR results. The other phase constituting the island is believed to be $Na_2Zr_2Si_2PO_{12}$. The Q^4 unit may have been formed by the exclusion of excess SiO_2 during the initial droplet phase separation in the crystal growth process. Excess Si is ejected during crystallization; however, because of low modifier contents, it exhibits high viscosity and limited diffusion. Therefore, it has a spinodal-like morphology within the crystals, as shown in Fig. 9. The spherical droplets (Fig. 9 (b) and (c)) are surrounded by a P- and Si-rich glass phase, suggesting that the spherical internal phases are composed of NASICON crystals and SiO_2-dominant glass. After $Na_2Zr_2Si_2PO_{12}$ is completely crystalized, the average composition of the remaining glass becomes $31Na_2O–33.3P_2O_5–35.6SiO_2$, with the SiO_2-rich glass and $Na_2O–P_2O_5$-rich glass primarily existing inside the droplets and sea phase, respectively.

In summary, we propose the crystal growth model shown in Fig. 11.

1) Droplets of 5 µm in diameter are formed and undergo a binodal phase separation. The separated phases are a few nanometers wide (Fig. 11 (a)). The droplets with a size of 300 nm separate into several nano-sized phases.
2) NZSP crystals with spinodal-like structures and widths of 50 nm are formed, whereas excess SiO_2 is expelled as Q^4 units on the island (Fig. 11 (b)).
3) The striped pattern is divided into spheres approximately 5 µm in diameter with a spinodal-like phase-separated morphology (Fig. 11 (c)).

3.4. Na-ion conductivity

The ionic conductivities at each temperature and the calculated activation energies are listed in Table 5. The Arrhenius plots are shown in Fig. 12. The ion conductivity at 300 K was 1.01×10^{-8} S·cm^{-1} for the non-heat-treated samples and up to 4.90×10^{-5} S·cm^{-1} for the crystallized samples. Ionic conductivity increased with increasing heat-treatment temperature even before crystallization (820 and 880 °C)
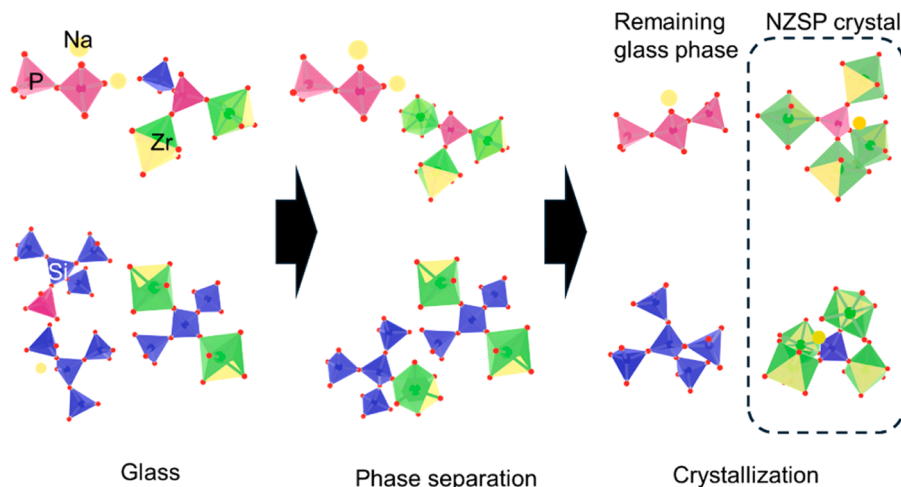

Fig. 8. Illustration of structural changes in the glass during heat-treatment.
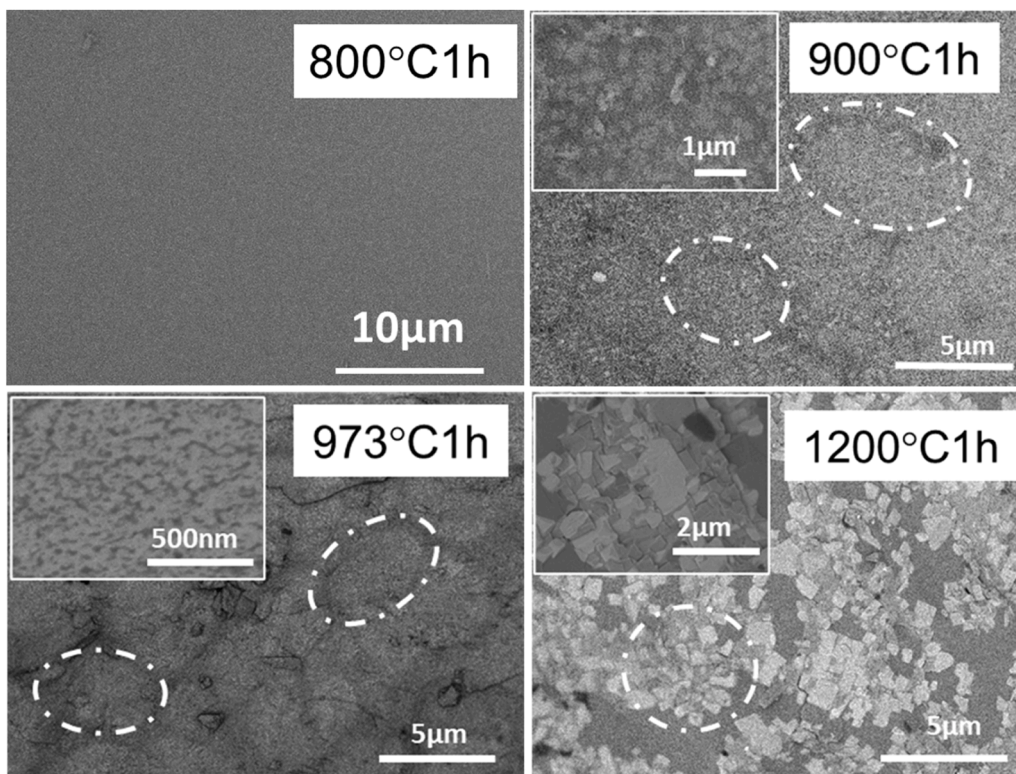
Fig. 9. SEM backscattered electron images of glass samples heat-treated at 800, 900, 973, and 1200 °C. High-magnification SEM images are shown in the insets.
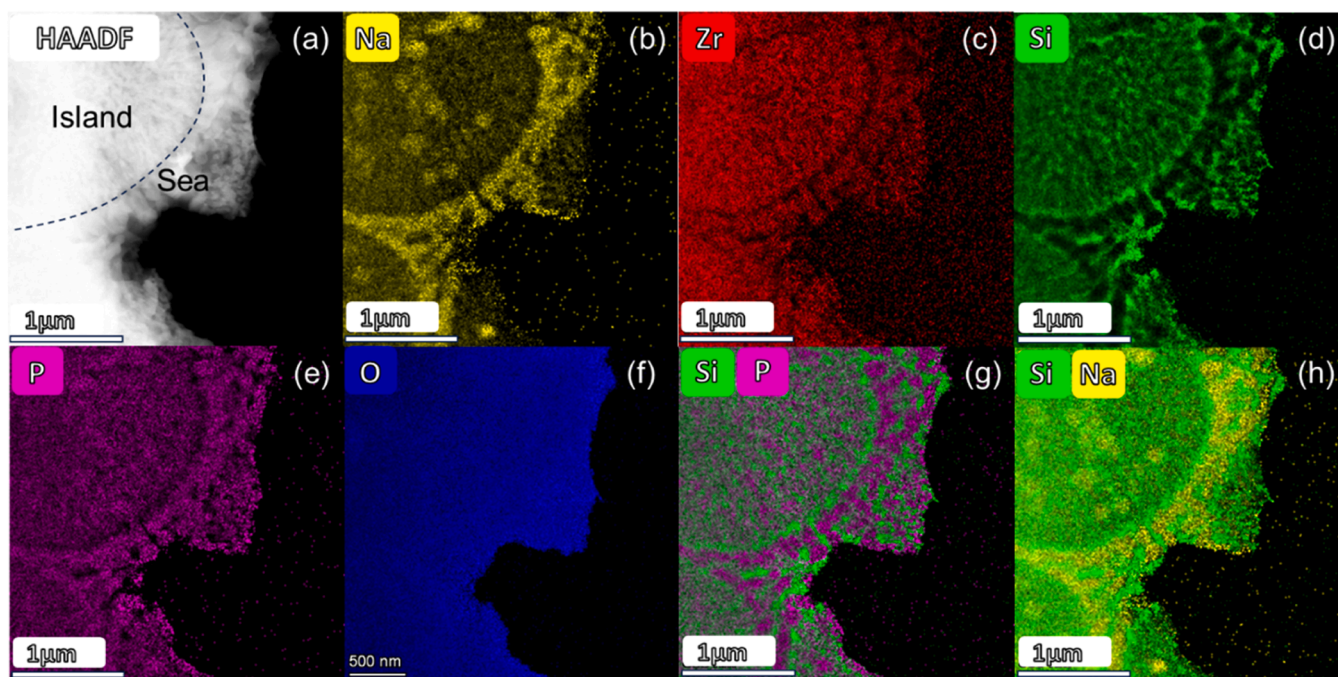

Fig. 10. (a) Dark-field STEM image, (b–f) EDS maps for Na, Zr, Si, P, and O, and a composite image of (g) Si and P and (h) Si and Na for the sample heat-treated at 1060 °C.

owing to phase separation. The ionic conductivity of $Na_2Zr_2SiP_2O_{12}$ is 6.6×10^{-5} S·cm^{-1} at 300 K [14], which is one magnitude less than that of a $Na_3Zr_2Si_2PO_{12}$ crystal (5.6×10^{-4} S·cm^{-1}). The ionic conductivity of the heat-treated sample was slightly lower than that of $Na_2Zr_2SiP_2O_{12}$, which can be attributed to the isolation of the crystals by the remaining Na–P-rich glass phase.

A CV experiment was conducted to investigate the water-leakage feature of the prepared materials (Fig. 13). If the water molecules pass through the prepared samples and reach the surface of the working electrode, the reduction current will appear at an electrochemical potential below 2.0 V vs. Na^+/Na owing to the reduction decomposition of water. Namely, a large reduction current indicates large water leakage
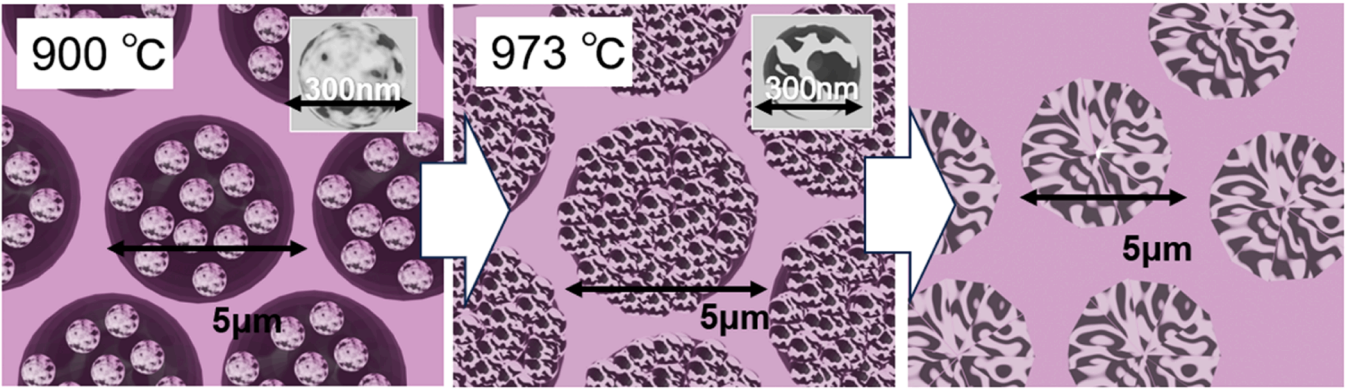
Fig. 11. Illustration of the crystal growth model. The pink areas are the Na- and P-rich sea phase, and the gray areas are the island phase. In the island phase, NZSP crystals and Si-rich glass phase are present in a spinodal morphology.

Table 5

Ionic conductivities and active energies of the glass before and after heat-treatment at 820, 880, 945, and 1060 °C for 1 h, measured at 300 K. The estimated standard uncertainty for the conductivity values is less than 5 %.

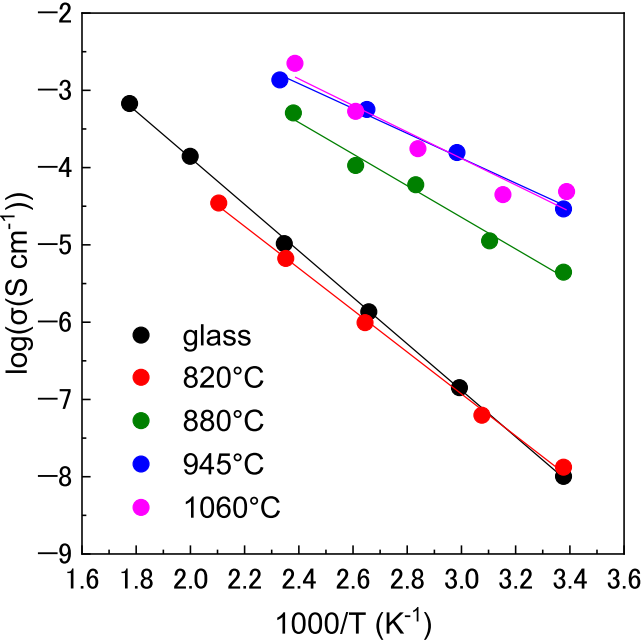| Heat-treatment condition	Ion conductivity at 300 K (S·cm^{-1})	Activation energy (eV)
As-received glass	1.0×10^{-8}	0.63
820 °C, 1 h	1.3×10^{-8}	0.57
880 °C, 1 h	4.4×10^{-6}	0.44
945 °C, 1 h	2.9×10^{-5}	0.35
1060 °C, 1 h	4.9×10^{-5}	0.37

Fig. 12. Arrhenius plot for ion conductivity of glass samples and heat-treated samples at 820, 880, 945, and 1060 °C for 1h. Estimated standard uncertainty for the values is less than 5 %.

Fig. 13. CV curves of the glass samples before and after heat-treatment at 880 and 973 °C for 1 h.

through the prepared samples. The glass exhibited high water resistance because it contained no flaws through which water could pass, and almost no leaks were detected. The glass-ceramics also exhibited good water resistance. Slight leaks could be attributed to the phosphate phase, which often has low water resistance. Recently, we succeeded in fabricating a NASICON material with a conductivity of 5.4×10^{-5} S·cm^{-1} at 300 K and leakage of -30 mA at 0.2 V vs. Na$^+$/Na, by improving the
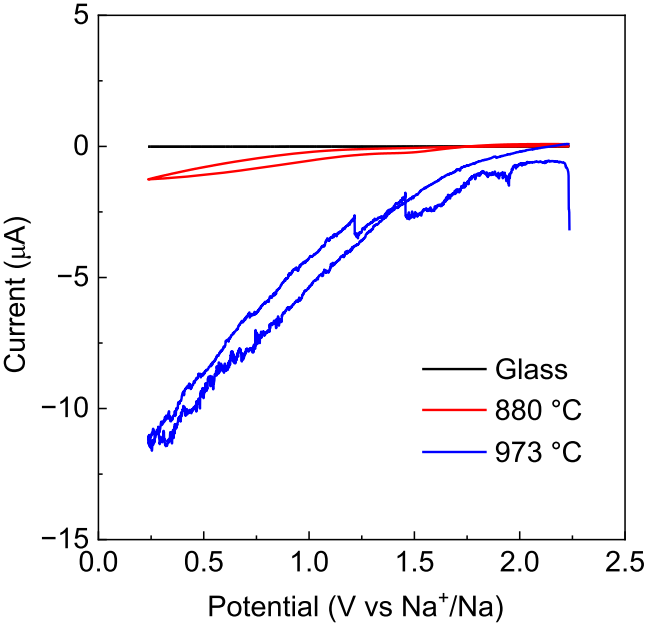
relative density of the material using appropriate sintering additives [10]. By contrast, simple sintered NASICON materials exhibit large leakage of -30 mA at 0.2 V [12]. Low-leakage NASICON materials have been successfully used as a separator in A-SIBs to achieve a cell voltage of 2.4 V using a Na$_3$LiTi$_5$O$_{12}$ negative electrode and 3 wt % H$_2$O$_2$ with a 1.0 M Na$_2$SO$_4$ aqueous electrolyte and 1.0 M NaTFSA-based nonaqueous electrolyte. The glass-ceramics have the same magnitude of water resistance. We believe that glass-ceramics can also be used in A-SIBs if their conductivity and leakage characteristics are slightly improved. We plan to pursue further improvements in the future because glass crystallization can be used to realize a flexible large-area separator.

4. Conclusion

In this study, we investigated the structure, crystal morphology, and crystallization mechanism of Na$_2$O–ZrO$_2$–P$_2$O$_5$–SiO$_2$–type crystalline glasses. We inferred the structural evolution and crystallization pathway of the material using GNN-MD simulations and ^{31}P and ^{29}Si-MAS-NMR, SEM, and (S)TEM observations. A model of glass structure and crystal morphogenesis during the heat-treatment crystallization process is proposed. Glass in a homogeneous state crystallizes upon heat-treatment

by forming 5 μm droplet phases and separating into spinodal morphology of $Na_2Zr_2SiP_2O_{12}$ (rhombohedral phase) crystals and Q^4 silica-rich glass in the droplets, which are surrounded by an alkaline phosphate-rich sea. In the glass, Zr forms isolated ZrO_4 tetrahedral units similar to the crystals, which hardly changes throughout crystallization. Si forms Q^2 and Q^3 units in the glassy state and crystallizes by forming a spinodal morphology with a width of a few nanometers in the droplet phase as it separates into the crystals and Q^4 state. P form Q^0 units in the glass and is linked to a small number of Zr units. With heat-treatment, the phosphate units increase in the number of linkages with Zr and separate into a crystalline phase and an alkaline phosphate-rich phase with more Q^n as a sea phase. Eventually, the crystals and Q^4 silica-rich phases appear with a spinodal morphology in the alkaline phosphate-rich sea and island phases. The ionic conductivity at 300 K increased with heat-treatment from 1.0×10^{-8} S·cm^{-1} for glass and to 4.9×10^{-5} S·cm^{-1} for glass-ceramics. The leakage tests showed that both glass and heat-treated glass exhibited small leakage. The leakage values are within the permissible limits of an A-SIB. Low leakage can be achieved by modifying the composition and structure of the residual glass phase, which exhibits insufficient water resistance.

Funding Sources

CRediT authorship contribution statement

Kento Sakaeda: Writing – review & editing, Writing – original draft, Visualization, Validation, Investigation, Formal analysis, Conceptualization. **Kenji Shinozaki:** Writing – review & editing, Writing – original draft, Validation, Supervision, Resources, Project administration, Funding acquisition, Formal analysis, Conceptualization. **Mitsunori Kitta:** Investigation, Formal analysis, Conceptualization. **Yuuki Kitagawa:** Investigation, Formal analysis. **Sohei Sukenaga:** Investigation, Formal analysis. **Tsuyoshi Honma:** Investigation, Funding acquisition, Formal analysis.

Declaration of competing interest

The authors declare that they have no known competing financial interests or personal relationships that could have appeared to influence the work reported in this paper.

Data availability

Data will be made available on request.

Acknowledgment

References

[1] C. Vaalma, D. Buchholz, M. Weil, S. Passerini, A cost and resource analysis of sodium-ion batteries, Nat. Rev. Mater. 3 (2018) 18013, https://doi.org/10.1038/natrevmats.2018.13.

[2] N. Yabuuchi, K. Kubota, M. Dahbi, S. Komaba, Research development on sodium-ion batteries, Chem. Rev. 114 (2014) 11636–11682, https://doi.org/10.1021/cr500192f.

[3] S.M. Hwang, J.S. Park, Y. Kim, W. Go, J. Han, Y. Kim, Y. Kim, Rechargeable seawater batteries—From concept to applications, Adv. Mater. 31 (2019) 1804936, https://doi.org/10.1002/adma.201804936.

[4] Z. Hou, X. Zhang, X. Li, Y. Zhu, J. Liang, Y. Qian, Surfactant widens the electrochemical window of an aqueous electrolyte for better rechargeable aqueous sodium/zinc battery, J. Mater. Chem. A 5 (2017) 730–738, https://doi.org/10.1039/c6ta08736a.

[5] T. Lv, L. Suo, Water-in-salt widens the electrochemical stability window: Thermodynamic and kinetic factors, Curr. Opin. Electrochem. 29 (2021) 100818, https://doi.org/10.1016/j.coelec.2021.100818.

[6] D. Reber, R. Grissa, M. Becker, R.S. Kühnel, C. Battaglia, Anion selection criteria for water-in-salt electrolytes, Adv. Energy Mater. 11 (2021), https://doi.org/10.1002/aenm.202002913, 2002913.

[7] L. Suo, O. Borodin, T. Gao, M. Olguin, J. Ho, X. Fan, C. Luo, C. Wang, K. Xu, Water-in-salt" electrolyte enables high-voltage aqueous lithium-ion chemistries, Science 350 (2015) 938–943, https://doi.org/10.1126/science.aab1595.

[8] V. Palomares, M. Casas-Cabanas, E. Castillo-Martínez, M.H. Han, T. Rojo, Update on Na-based battery materials. A growing research path, Energy Environ. Sci. 6 (2013) 2312, https://doi.org/10.1039/c3ee41031e.

[9] K. Nakamoto, R. Sakamoto, Y. Sawada, M. Ito, S. Okada, Over 2 V aqueous sodium-ion battery with Prussian Blue-type electrodes, Small Methods 3 (2019) 3–7, https://doi.org/10.1002/smtd.201800220.

[10] M. Kitta, R. Kataoka, S. Tanaka, N. Takeichi, M. Kohyama, Spinel-type sodium titanium oxide: A promising sodium-insertion material of sodium-ion batteries, ACS Appl. Energy Mater. 2 (2019) 4345–4353, https://doi.org/10.1021/acsaem.9b00541.

[11] L. Fan, S. Wei, S. Li, Q. Li, Y. Lu, Recent progress of the solid-state electrolytes for high-energy metal-based batteries, Adv. Energy Mater. 8 (2018) 1702657, https://doi.org/10.1002/aenm.201702657.

[12] M. Kitta, K. Sakaeda, K. Shinozaki, K. Mitsunori, S. Kento, S. Kenji, Preparation of water–impermeable NASICON solid electrolyte separators for aqueous/nonaqueous hybrid sodium-ion cells using alumina as a sintering aid, J. Alloys Compd. 969 (2023) 172494, https://doi.org/10.1016/j.jallcom.2023.172494.

[13] J.B. Goodenough, H.Y.P. Hong, J.A. Kafalas, Fast Na$^+$-ion transport in skeleton structures, Mater. Res. Bull. 11 (1976) 203–220, https://doi.org/10.1016/0025-5408(76)90077-5.

[14] H.Y.P. Hong, Crystal structures and crystal chemistry in the system Na$_{1+}$$_xZr_2Si_xP_{3-x}O_{12}$, Mater. Res. Bull. 11 (1976) 173–182, https://doi.org/10.1016/0025-5408(76)90073-8.

[15] T. Honma, M. Okamoto, T. Togashi, N. Ito, K. Shinozaki, T. Komatsu, Electrical conductivity of Na$_2$O–Nb$_2$O$_5$–P$_2$O$_5$ glass and fabrication of glass–ceramic composites with NASICON type Na$_3$Zr$_2$Si$_2$PO$_{12}$, Solid State Ionics 269 (2015) 19–23, https://doi.org/10.1016/j.ssi.2014.11.009.

[16] S. Susman, C. Delbecq, J. Mcmillan, M. Roche, NASIGLAS: A new vitreous electrolyte, Solid State Ionics 9–10 (1983) 667–673, https://doi.org/10.1016/0167-2738(83)90312-0.

[17] A. Niyompan, D. Holland, NASIGLAS structure and properties, J. Non-Cryst. Solids 293–295 (2001) 709–714, https://doi.org/10.1016/S0022-3093(01)00781-5.

[18] S. Morimoto, Ionic conductivity of Na$_2$O-ZrO$_2$-P$_2$O$_5$-SiO$_2$ system glass ceramic, J. Ceram. Soc. Jpn. 97 (1989) 1097–1103, https://doi.org/10.2109/jcersj.97.1097 [in Japanese].

[19] J. Deubener, Structural aspects of volume nucleation in silicate glasses, J. Non-Cryst. Solids 351 (2005) 1500–1511, https://doi.org/10.1016/j.jnoncrysol.2004.04.028.

[20] T. Komatsu, Design and control of crystallization in oxide glasses, J. Non-Cryst. Solids 428 (2015) 156–175, https://doi.org/10.1016/j.jnoncrysol.2015.08.017.

[21] K. Shinozaki, Y. Ishii, S. Sukenaga, K. Ohara, Ultrafast nanocrystallization of BaF$_2$ in oxyfluoride glasses with crystal-like nanostructures: Implications for upconversion fiber devices, ACS Appl. Nano Mater. 5 (2022) 4281–4292, https://doi.org/10.1021/acsanm.2c00205.

[22] K. Shinozaki, Design of crystallization of oxyfluoride glasses based on the local structure of fluorine, J. Ceram. Soc. Jpn. 126 (2018) 684–692, https://doi.org/10.2109/jcersj2.18102.

[23] K. Shinozaki, H. Tsuchiya, T. Honma, K. Ohara, H. Masai, T. Ina, T. Komatsu, Structural origin of high-density Gd$_2$O$_3$–MoO$_3$–B$_2$O$_3$ glass and low-density β′-Gd$_2$(MoO$_4$)$_3$ crystal: A study conducted using high-energy X-ray diffraction and EXAFS at high temperatures, J. Phys. Condens. Matter 32 (2020) 055705, https://doi.org/10.1088/1361-648X/ab4e64.

[24] C. Chen, S.P. Ong, A universal graph deep learning interatomic potential for the periodic table, Nat. Comput. Sci. 2 (2022) 718–728, https://doi.org/10.1038/s43588-022-00349-3.

[25] K. Momma, F. Izumi, *VESTA3* for three-dimensional visualization of crystal, volumetric and morphology data, J. Appl. Crystallogr. 44 (2011) 1272–1276, https://doi.org/10.1107/S0021889811038970.

[26] A.P. Thompson, H.M. Aktulga, R. Berger, D.S. Bolintineanu, W.M. Brown, P.S. Crozier, P.J. in ʼt Veld, A. Kohlmeyer, S.G. Moore, T.D. Nguyen, R. Shan, M.J. Stevens, J. Tranchida, C. Trott, S.J. Plimpton, LAMMPS – a flexible simulation tool for particle-based materials modeling at the atomic, meso, and continuum scales, Comput. Phys. Commun. 271 (2022) 108171, https://doi.org/10.1016/j.cpc.2021.108171.

[27] K. Hirao, K. Kawamura, Pasokon ni yoru Zairyo Sekkei (material design using a personal computer) (Syoka-bo, Tokyo) (1994) [in Japanese].

[28] W. Baur, J. Dygas, D. Whitmore, J. Faber, Neutron powder diffraction study and ionic conductivity of Na$_2$Zr$_2$SiP$_2$O$_{12}$ and Na$_3$Zr$_2$Si$_2$PO$_{12}$, Solid State Ionics 18–19 (1986) 935–943, https://doi.org/10.1016/0167-2738(86)90290-0.

[29] J. Didisheim, E. Prince, B. Wuensch, Neutron Rietveld analysis of structural changes in NASICON solid solutions $Na_{1+x}Zr_2Si_xP_{3-x}O_{12}$ at elevated temperatures: x=1.6 and 2.0 at 320°C, Solid State Ionics 18–19 (1986) 944–958, https://doi.org/10.1016/0167-2738(86)90291-2.

[30] N.G. Bukun, Superionic transitions in NASICON-type solid electrolytes, Ionics 2 (1996) 63–68, https://doi.org/10.1007/BF02375870.

[31] U. von Alpen, M.F. Bell, W. Wichelhaus, Phase transition in NASICON $(Na_3Zr_2Si_2PO_{12})$, Mater. Res. Bull. 14 (1979) 1317–1322, https://doi.org/10.1016/0025-5408(79)90010-2.

[32] K. Shinozaki, K. Hashimoto, T. Honma, T. Komatsu, TEM analysis for crystal structure of metastable $BiBO_3$ (II) phase formed in glass by laser-induced crystallization, J. Eur. Ceram. Soc. 35 (2015) 2541–2546, https://doi.org/10.1016/j.jeurceramsoc.2015.03.020.

[33] K. Shinozaki, T. Honma, M. Affatigato, T. Komatsu, Long afterglow in hexagonal $SrAl_2O_4:Eu^{2+}$, Dy^{3+} synthesized by crystallization of glass and solidification of supercooled melts, J. Lumin. 177 (2016) 286–289, https://doi.org/10.1016/j.jlumin.2016.05.013.

[34] M.R. Cicconi, R. Belli, M. Brehl, J. Lubauer, T. Hayakawa, K. Kimura, T. Hirota, K. Usui, S. Kohara, Y. Onodera, U. Lohbauer, K. Hayashi, D. de Ligny, Nucleation mechanisms in a SiO_2-Li_2O-P_2O_5-ZrO_2 biomedical glass-ceramic: Insights on crystallisation, residual glasses and Zr^{4+} structural environment, J. Eur. Ceram. Soc. 42 (2022) 1762–1775, https://doi.org/10.1016/j.jeurceramsoc.2021.12.009.

[35] T.J. Bastow, M.E. Hobday, M.E. Smith, H.J. Whitfield, Solid state NMR characterisation of crystalline Na_2O-ZrO_2-SiO_2 phases, Solid State Nucl. Magn. Reson. 5 (1996) 293–303, https://doi.org/10.1016/0926-2040(95)01198-6.

[36] Z. Lin, J. Rocha, P. Ferreira, A. Thursfield, J.R. Agger, M.W. Anderson, Synthesis and structural characterization of microporous framework zirconium silicates, J. Phys. Chem. B 103 (1999) 957–963, https://doi.org/10.1021/jp983708x.

[37] H. Maekawa, T. Maekawa, K. Kawamura, T. Yokokawa, The structural groups of alkali silicate glasses determined from ^{29}Si MAS-NMR, J. Non-Cryst. Solids 127 (1991) 53–64, https://doi.org/10.1016/0022-3093(91)90400-Z.

[38] C. Jäger, G. Scheler, U. Sternberg, S. Barth, A. Feltz, ^{29}Si and ^{31}P MAS NMR study of the NASICON system $Na_{1+x}Zr_2(PO_4)_x(PO_4)_{3-x}$, Chem. Phys. Lett. 147 (1988) 49–52, https://doi.org/10.1016/0009-2614(88)80222-7.

[39] X. Xue, J.F. Stebbins, ^{23}Na NMR chemical shifts and local Na coordination environments in silicate crystals, melts and glasses, Phys. Chem. Miner. 20 (1993) 297–307, https://doi.org/10.1007/BF00215100.

[40] O.B. Lapina, D.F. Khabibulin, V.V. Terskikh, Multinuclear NMR study of silica fiberglass modified with zirconia, Solid State Nucl. Magn. Reson. 39 (2011) 47–57, https://doi.org/10.1016/j.ssnmr.2010.12.002.

[41] R.K. Brow, R.J. Kirkpatrick, G.L. Turner, The short range structure of sodium phosphate glasses I. MAS NMR studies, J. Non-Cryst. Solids 116 (1990) 39–45, https://doi.org/10.1016/0022-3093(90)91043-Q.

[42] V. Kahlenberg, B. Marler, J.C. Muñoz Acevedo, J. Patarin, Ab initio crystal structure of $Na_2Si_3O_7$ from conventional powder diffraction data, Solid State Sci 4 (2002) 1285–1292, https://doi.org/10.1016/S1293-2558(02)00006-7.

[43] E. Lissel, M. Jansen, E. Jansen, G. Will, Bestimmung der Kristallstruktur von T-Na_3PO_4 mit Röntgen- und Neutronenpulvertechniken, Z. Kristallogr. Cryst. Mater. 192 (1990) 233–243, https://doi.org/10.1524/zkri.1990.192.3-4.233.

[44] T.M. Duncan, D.C. Douglas, On the ^{31}P chemical shift anisotropy in condensed phosphates, Chem. Phys. 87 (1984) 339–349, https://doi.org/10.1016/0301-0104(84)85115-0.

[45] S. Shen, B. Tian, C. Yu, S. Xie, Z. Zhang, B. Tu, D. Zhao, Synthesis of highly ordered thermally stable cubic mesostructured zirconium Oxophosphate templated by tri-headgroup quaternary ammonium surfactants, Chem. Mater. 15 (2003) 4046–4051, https://doi.org/10.1021/cm0342389.

[46] I.J. King, R.K. Harris, J.S.O. Evans, F. Fayon, D. Massiot, A space group assignment of ZrP_2O_7 obtained by ^{31}P solid state NMR, Chem. Commun. 18 (2001) 1766–1767, https://doi.org/10.1039/b106379k.